

Relaxation Digital-to-Analog Converters Featuring Self-Calibration and Parasitics-Induced Error Suppression in 180-nm CMOS

Original

Relaxation Digital-to-Analog Converters Featuring Self-Calibration and Parasitics-Induced Error Suppression in 180-nm CMOS / Rubino, R.; Musolino, F.; Leite Correia de Toledo, P.; Chen, Y.; Richelli, A.; Crovetti, P. S.. - In: IEEE ACCESS. - ISSN 2169-3536. - ELETTRONICO. - 13:(2025), pp. 6594-6605. [10.1109/ACCESS.2025.3526209]

Availability:

This version is available at: 11583/2997521 since: 2025-02-14T15:30:13Z

Publisher:

Institute of Electrical and Electronics Engineers

Published

DOI:10.1109/ACCESS.2025.3526209

Terms of use:

This article is made available under terms and conditions as specified in the corresponding bibliographic description in the repository

Publisher copyright

(Article begins on next page)

RESEARCH ARTICLE

Relaxation Digital-to-Analog Converters Featuring Self-Calibration and Parasitics-Induced Error Suppression in 180-nm CMOS

ROBERTO RUBINO¹, (Member, IEEE), FRANCESCO MUSOLINO², (Member, IEEE), PEDRO TOLEDO³, (Member, IEEE), YONG CHEN⁴, (Senior Member, IEEE), ANNA RICHELLI⁵, (Senior Member, IEEE), AND PAOLO S. CROVETTI², (Senior Member, IEEE)

¹Analog Devices, 70021 Bari, Italy

²Department of Electronics and Telecommunications (DET), Politecnico di Torino, 10129 Turin, Italy

³Synopsys, 2740-267 Lisbon, Portugal

⁴Department of Electronic Engineering, Tsinghua University, Beijing 100084, China

⁵Department of Information Engineering, University of Brescia, 25123 Brescia, Italy

Corresponding author: Paolo S. Crovetti (paolo.crovetti@polito.it)

ABSTRACT The design and the silicon characterization of two mostly digital, low-voltage, energy- and area-efficient Relaxation Digital-to-Analog Converters (ReDACs) in 180 nm featuring digital self-calibration and parasitics-induced error suppression are presented and compared in this paper. The first design is a single-ended ReDAC (SE-ReDAC) and operates at 880 kS/s with a 10-bit resolution, while the second is based on a differential ReDAC (Diff-ReDAC) architecture and operates at 100 kS/s with a 13-bit resolution. The SE-ReDAC testchip in 180nm occupies just $5,030 \mu\text{m}^2$ and operates with a supply voltage ranging from 0.6 V to 1 V. Experimental results at 0.65 V reveal a 72.18 dB-SFDR, a 65.59 dB-THD and a 56.09 dB SINAD, resulting in 9.02 ENOB, with a power dissipation of just $3.3 \mu\text{W}$, achieving a competitive energy-efficiency (area-normalized energy efficiency) figure of merit FOM (FOM_A) of 166 dB (175 dB). On the other hand, the 180-nm Diff-ReDAC testchip occupies $7,800 \mu\text{m}^2$ and operates in a supply voltage range from 0.45 V to 1 V, while achieving a 77.81 dB-SFDR, a 77.52 dB-THD and a 65.82 dB-SINAD (10.64 ENOB) at 0.6 V supply with a power consumption of just 880 nW, leading to a very competitive FOM (FOM_A) of 172 dB (178 dB).

INDEX TERMS D/A converter (DAC), relaxation D/A converter (ReDAC), ultra-low area, digital-based, ultra-low power, ultra-low voltage, Internet of Things (IoT), biosensors.


I. INTRODUCTION

Emerging harvester-powered Internet of Things (IoT) nodes [1], [2] and micrometer-scale biosensors [3] demand extremely compact, low-power, low-cost integrated circuits operating at supply voltages well below 1 V [4].

In this context, Digital-to-Analog (D/A) converters (DACs) with a sub- μW power budget, an effective resolution in the 10-bit range and a bandwidth from the kHz up to the

MHz range are needed in wearable and implantable biosensors for electrochemical impedance spectroscopy (EIS) and cyclic voltammetry [5], [6], [7], [8], [9], [10]. DACs with comparable performance and power budget are required in energy autonomous IoT sensor nodes for on-chip automatic tuning/calibration, audio processing and threshold generation for event detection, among the others [1], [11], [12].

Since these specifications are extremely challenging for traditional analog and mixed-signal (AMS) integrated circuit (IC) design, new digital-based DACs [11], [12], [13], [14], [15], [16], [17], [18], [19] have been proposed in the last years

The associate editor coordinating the review of this manuscript and approving it for publication was Woorham Bae .

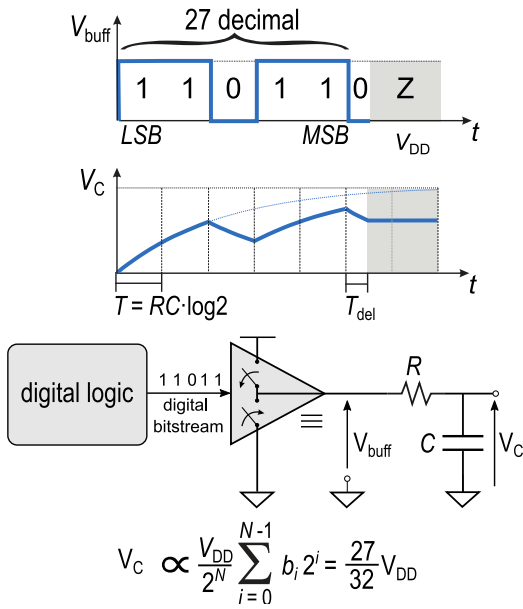


FIGURE 1. ReDAC concept and operating principle.

to address the needs of emerging applications at low cost and design effort.

In this framework, the Relaxation Digital-to-Analog converter (ReDAC) has been introduced in [15] and validated on FPGA and by simulations in 40 nm [20]. From these works, the potential of ReDACs has clearly emerged, even if the early prototypes required impractical manual clock frequency calibration, and their accuracy was severely limited by parasitics. Aiming to address these limitations, a ReDAC self-calibration technique was proposed in [17], but its effectiveness was validated by simulations only, and the ReDAC performance was still limited by parasitics. In [16], a simple parasitics-induced error suppression strategy, which dramatically enhances the ReDAC accuracy, was introduced and demonstrated on an FPGA prototype, which also features automatic clock frequency calibration. Neither the parasitics-induced error suppression nor the automatic calibration, however, have been validated on silicon to date.

In this work, which extends our preliminary conference paper [19], the implementation in 180 nm CMOS of two ReDACs featuring both parasitics-induced error suppression and digital on-chip self-calibration is addressed. The first converter, SE-ReDAC, is based on a single-ended architecture and operates at 880 kS/s with a 10-bit resolution, while the second, Diff-ReDAC, is based on a differential architecture and operates at 100 kS/s targeting a 13-bit resolution.

The rest of the paper is organized as follows: the ReDAC operation is reviewed in Sect. II, while the design of the SE-ReDAC and of the Diff-ReDAC cores are discussed in Sect. III, where the first on-chip implementation of the parasitics-induced error suppression strategy and of the on-chip self-calibration are described in detail. The architecture of the test-chip is introduced in Sect. IV, and the experimental

test results are then presented and compared with the state of the art in Sect. V. Some concluding remarks are finally drawn in Sect. VI.

II. THE RELAXATION DAC (REDAC)

The ReDAC operation [15] and the background about ReDAC clock frequency self-calibration and parasitics-induced error suppression [16] are revised in this Section to introduce the silicon implementation presented in this paper.

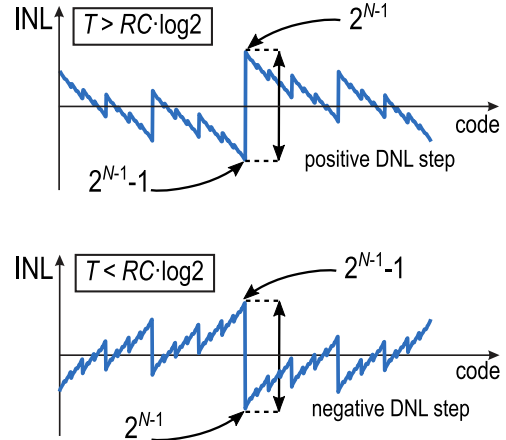


FIGURE 2. ReDAC Integral Non-Linearity (INL) error due to the deviation of the ReDAC clock period T from its nominal value $T^* = RC \log 2$.

A. REDAC PRINCIPLE

As illustrated in Fig.1, a ReDAC is made up of a simple three-state digital buffer that drives a first-order low-pass RC network for a period $t \in [0, NT]$ with a stream of N rectangular pulses with equal duration T and amplitude $b_i V_{DD}$, that can be either 0 or V_{DD} , depending on the logical value of the bits $\{b_{N-1} \dots b_0\}$ in the digital input code

$$n = \sum_{i=0}^{N-1} b_i 2^i, \quad (1)$$

streamed out from the LSB, b_0 , to the MSB, b_{N-1} .

Assuming a zero initial condition ($v_C(0) = 0$ V) and imposing the continuity of v_C at each clock transition, the evolution of the capacitor voltage $v_C(t)$ can be evaluated by first-order transient analysis and its final value $v_C(NT)$ at the end of the conversion can be expressed as [15]

$$v_C(NT) = V_{DD} \left(1 - e^{-\frac{T}{\tau}}\right) \sum_{i=0}^{N-1} b_i e^{-\frac{(N-1-i)T}{\tau}}. \quad (2)$$

If the time constant $\tau = RC$ and the pulse duration T are related to each other so that

$$e^{-\frac{T}{\tau}} = \frac{1}{2} \implies T = \tau \log 2 = T^* \quad (3)$$

based on (2), the final capacitor voltage is proportional to the binary value of the digital input code n

$$v_C(NT^*) = \frac{V_{DD}}{2^N} \sum_{i=0}^{N-1} b_i 2^i = \frac{n}{2^N} V_{DD} = V_{DAC}(n), \quad (4)$$

as expected in a DAC.

B. REDAC CLOCK PERIOD CALIBRATION

When the ReDAC clock period T varies from its nominal value T^* , e.g. because of process, supply voltage and temperature (PVT) variations in the clock source, the ReDAC transfer curve is affected by a nonlinearity error that increases with the clock period deviation $\Delta T = T - T^*$. As a consequence, the condition (3) needs to be enforced by calibration at an accuracy related to the target linearity of the converter.

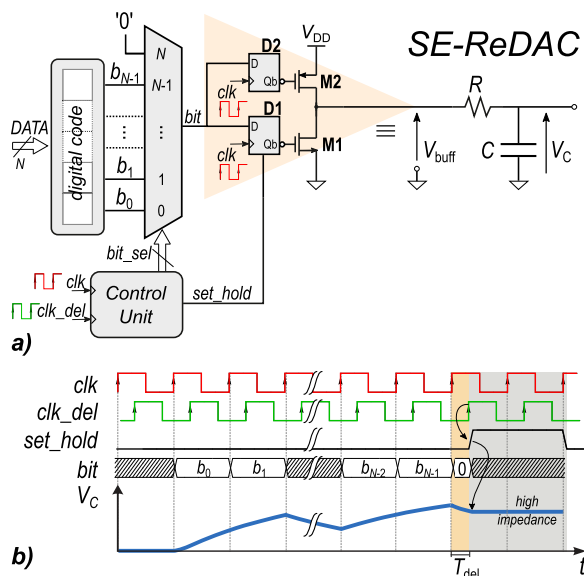


FIGURE 3. Architecture of the proposed SE-ReDAC.

The ReDAC clock period calibration is greatly simplified by the properties of the ΔT -related ReDAC differential nonlinearity (DNL) error highlighted in [16] and illustrated in Fig.2: since the ReDAC DNL is maximum in magnitude at mid-range, it is sufficient to enforce $\Delta V_{DAC} = V_{DAC}(2^{N-1}) - V_{DAC}(2^{N-1} - 1) = 0$ at the target resolution to guarantee a DNL below 1 LSB across the whole input range. Moreover, due to the monotonic dependence of the error on ΔT , the condition $\Delta V_{DAC} = 0$ can be enforced tuning the ReDAC clock period based on the sign of ΔV_{DAC} by a binary search algorithm [16], [17], [18].

The calibration approach outlined above has been originally demonstrated in [16] on an FPGA prototype, and its silicon implementation on the SE-ReDAC and Diff-ReDAC prototype will be discussed in Sect.III-D.

C. REDAC NON-IDEALITIES AND PARASITICS ERROR SUPPRESSION

Once the ReDAC clock period is calibrated so as to meet condition (3), the accuracy and performance of a real ReDAC are still limited by parasitics, noise, loading effect in the three-state buffer, finite rise and fall times and leakage currents in the hold phase. Such non-idealities have been shortly analyzed in [16], where it has been highlighted that the errors related to the higher-order time constants introduced by the parasitics of the RC network are by far the more relevant.

The dominant parasitics-induced error, however, can be effectively suppressed driving the three-state buffer low for a short time interval $T_{del} \ll \tau$ before the hold phase, making it possible to achieve a ReDAC effective resolution in the order of 10 bit and more. Such a parasitics-induced error suppression strategy was demonstrated on an FPGA prototype in [16] and its first silicon implementation in the SE-ReDAC and Diff-ReDAC test chips will be introduced in Sect.III-C. The other non-ideal effects will be considered in the design of the same ReDACs in Sect.III, so that to achieve optimal performance.

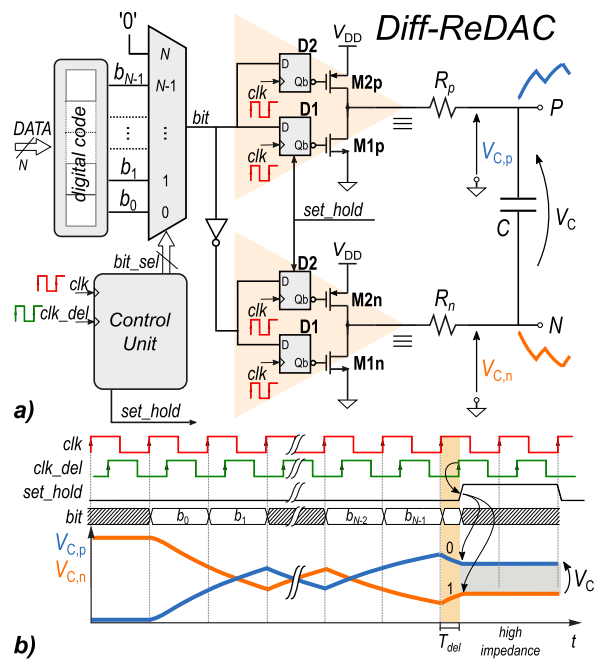


FIGURE 4. Architecture of the proposed Diff-ReDAC.

III. INTEGRATED REDACS DESIGN

The design in 180 nm CMOS of the 10-bit, 880 kS/s SE-ReDAC based on the architecture in Fig. 3 and of the 13-bit, 100 kS/s Diff-ReDAC in Fig. 4 is illustrated in what follows.

A. REDACS ARCHITECTURE

The SE-ReDAC architecture in Fig. 3 closely resembles the block diagram in Fig.1, in which the three-state buffer M1-M2 is driven by two D-flip flops (DFFs). On the other

hand, the Diff-ReDAC is based on the architecture in Fig.4, which entails an output stage made up of two three-state buffers (Buff_p and Buff_n) that drive a floating RC network ($R_p = R_n = R/2$ and C). The buffer Buff_p (Buff_n) is driven with the input code bitstream ($b_{N-1} \dots b_0$) (the complemented bitstream ($\bar{b}_{N-1} \dots \bar{b}_0$)) by the DFFs $D1_p$, $D2_p$ ($D1_n$, $D2_n$). After the MSB is processed, the DAC output $V_{\text{DAC}} = v_{C,p}(NT^*) - v_{C,n}(NT^*) = v_C(NT^*)$ is

$$V_{\text{DAC}} = 2 \frac{n}{2^N} V_{\text{DD}} - V_{\text{DD}} \quad (5)$$

and its value is hold across the capacitor by operating Buff_p (Buff_n) in high impedance.

B. RC NETWORK AND BUFFER DESIGN

In both ReDACs, the integrated RC network has been designed using high-resistivity polysilicon resistors (RHiPo) in view of their superior linearity, good stability over temperature and high sheet resistance. Similarly, Metal-Insulator-Metal (MIM) capacitors have been chosen in consideration of their linearity, low thermal drift and high specific capacitance.

Since the ReDAC energy per conversion, which can be expressed as a function of the digital code n as:

$$E(n) = CV_{\text{DD}}^2 \sum_{i=0}^{N-1} b_i \sum_{j=0}^i 2^{j-i} (b_j - b_{j-1}) \quad b_{-1} \triangleq 0. \quad (6)$$

scales linearly with the capacitance C and quadratically with the supply voltage V_{DD} , the ReDACs have been designed to operate at the lowest supply voltage compatible with the operation of the logic at the target sample rate, i.e.: 0.6 V for the SE-ReDAC, to allow operation at 880 kS/s and 0.4 V for the Diff-ReDAC, to allow operation at 100 kS/s.

Since the ReDAC accuracy is decided by the ratio T/τ and is independent of matching, both area and power are minimized reducing the capacitance C close to the thermal noise limit [15]. In consideration of that, the capacitance C of both the ReDACs has been designed to make the thermal noise power contribution $\kappa T/C$ negligible compared to the quantization noise power $V_{\text{DD}}^2/(12 \cdot 2^{2N})$ for the target N -bit resolution and at the minimum supply voltage.

Applying this criterium to our design, a capacitance of $C = 900$ fF ($C = 2.6$ pF) is chosen in the SE-ReDAC (Diff-ReDAC) to achieve a 10-bit resolution (a 13 bit resolution).

Once the capacitance C is fixed, the resistance R of the RC network is designed in consideration of the time constant needed to meet the ReDAC condition (3) at the target sample rate $F_{\text{conv}} = 1/T_{\text{conv}}$, i.e. imposing

$$T_{\text{conv}} = (N + K)T^* = (N + K)\tau \log 2 \quad (7)$$

in which N are the clock cycles required for the conversion and $K = 3$ are the extra cycles needed for parasitics-induced error suppression and for the hold phase. In the SE-ReDAC, since $N = 10$, imposing a $880 \text{ kS/s} = T_{\text{conv}}^{-1}$ sample rate, a time constant $\tau = 126$ ns and hence a resistance

$R = 140 \text{ k}\Omega$ are derived from (7). By a similar approach, a resistance $R = 360 \text{ k}\Omega$ is obtained for the Diff-ReDAC imposing a 100 kS/s sample time. Such a resistance has been split into two identical resistors $R_p = R_n = R/2 = 180 \text{ k}\Omega$ connected at the non-inverting and inverting outputs for symmetry.

The strength of the output buffer has been optimized based on simulations so that to keep the DNL degradation due to the non-linearity in their ON drain-source resistance below 1 LSB. For the SE-ReDAC, this condition is met with an nMOS (pMOS) aspect ratio of $3.3 \mu\text{m}/0.18 \mu\text{m}$ ($6.6 \mu\text{m}/0.18 \mu\text{m}$). In the Diff-ReDAC, two output buffers driven by complementary signals are introduced for differential operation and their transistors $M1_p$ $M2_p$, $M1_n$ $M2_n$ have been designed with an equal aspect ratios of $5 \mu\text{m}/0.18 \mu\text{m}$.

C. DIGITAL DESIGN AND PARASITICS-INDUCED ERROR SUPPRESSION

The operations of the SE-ReDAC and Diff-ReDAC are orchestrated by a digital control unit, so as to drive the three-state output buffer(s) with the timing requested for the conversion and for suppressing the parasitics-induced error, as discussed in Sect.II-C. In details, the SE-ReDAC and Diff-ReDAC digital core timing diagrams are shown in Fig. 3b and in Fig. 4b, respectively. The control unit has been synthesized and laid out in a standard-cell digital flow, starting from a behavioral description in Very high speed integrated circuits Hardware Description Language (VHDL).

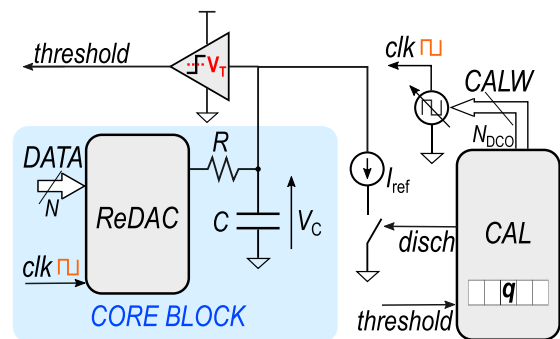


FIGURE 5. Calibration network architecture.

Compared to previous ReDACs [15], [16], [17], [18], in which a shift register was employed to serialize the input bits, in the SE-ReDAC and Diff-ReDAC cells presented in this paper the input code is sampled from the DATA bus and stored in a register, and its bits are streamed out in sequence, LSB-first, by a multiplexer (MUX) driven by the Control Unit. This results in a lower switching activity and hence in a reduced power consumption. For the same purpose, the Control Unit finite state machine is hard-coded as a Gray counter rather than as a binary counter.

To implement the parasitic error suppression technique described in Sect.II-C, the gates of the output buffer are driven by the standard-cell DFFs D1 and D2 operated at $f_{\text{clk}} = 1/T$, that are synchronously preset at the end of the conversion on

the rising edge of the clock signal, and then asynchronously reset at the rising edge of a delayed clock signal clk_del , so as to turn on the pull-down transistor of the output buffer for a time $T_{del} \ll T$ after the end of the conversion, and then set the three-state buffer in high impedance for the hold phase (see timing diagrams in Fig. 3b and Fig. 4b).

D. CALIBRATION

The self-calibration block (CAL) in Fig.5 is designed to tune the frequency of the clock, which is generated by a digitally-controlled oscillator (DCO) based on the sign of the difference $\Delta V_{DAC} = V_{DAC}(2^{N-1}) - V_{DAC}(2^N - 1)$ so as to implement the calibration procedure described in Sect.II-B and to enforce the linear operation condition (3).

In details, the calibration network includes a current sink driven by a pW-power reference [26], that can be enabled by the *disch* control signal to discharge the ReDAC output capacitance during the hold phase, a voltage comparator with threshold V_T , implemented as a CMOS inverter with power gating, and an up/down counter. All the calibration blocks are driven by the calibration control unit as illustrated in the flow chart in Fig.6 and described below.

at the center frequency of its tuning range. In the first calibration step, the ReDAC converts $V_{DAC}(2^{N-1} - 1)$. Then, during the hold phase the current sink is enabled to discharge the output capacitor at constant current till it crosses the comparator threshold V_T (see timing diagram in Fig.6). During the discharge, the counter q is set in up-count mode, and is incremented at each clock active edge so as to digitize the discharge time, as in a time-to-digital converter (TDC). In the second step, $V_{DAC}(2^N)$ is converted and the capacitor is then discharged decrementing the counter q until V_T is crossed. The sign of the counter word q at the end of one calibration cycle is therefore equal to the sign of $-\Delta V_{DAC}$ and $-\Delta T$, neglecting the counter quantization and the comparator noise. If $q = 0$, the ReDAC condition (3) is met within 1 LSB and the calibration is terminated. On the other hand, if $q \neq 0$ the calibration word $CALW \propto T$ is dichotomically increased (decreased) by a successive-approximation-register (SAR) logic if $q > 0$ ($q < 0$), and a new calibration cycle begins.

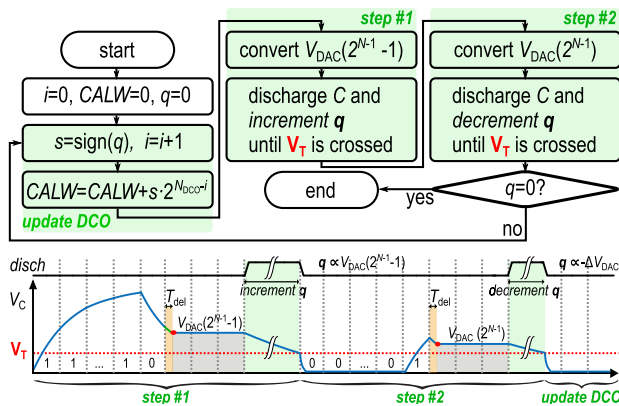


FIGURE 6. Calibration flowchart and timing diagram.

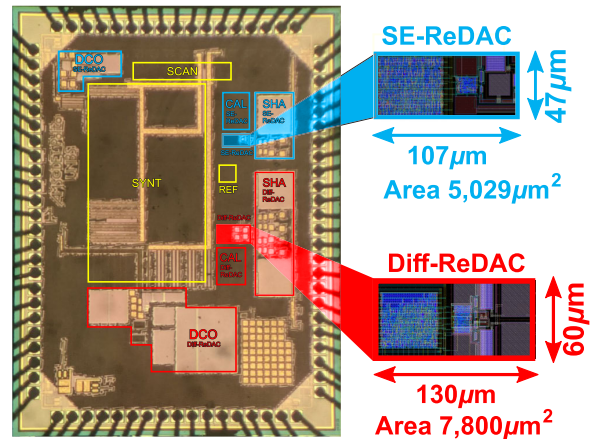


FIGURE 8. Chip micrograph.

TABLE 1. Area of SE-ReDAC and Diff-ReDAC cores and ancillary blocks in the 180 nm test chip in Fig.8.

SE-ReDAC			
Block	Area (μm^2)	Block	Area (μm^2)
Core	5,029	CAL	24,800
DCO	38,800	SHA	46,130
Diff-ReDAC			
Block	Area (μm^2)	Block	Area (μm^2)
Core	7,800	CAL	24,800
DCO	188,600	SHA	92,260
Other blocks			
Block	Area (μm^2)	Block	Area (μm^2)
SYNT	540,000	SCAN	37,600
REF	7,400		

IV. TEST-CHIP ARCHITECTURE

The SE-ReDAC and the Diff-ReDAC presented in this paper have been integrated in a 180 nm ReDAC test-chip whose block diagram is shown in Fig.7 and whose micrograph is

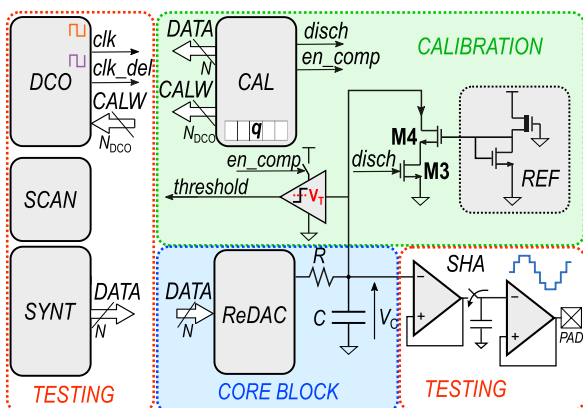


FIGURE 7. ReDAC Test-Chip architecture.

At the system reset, the $N_{DCO} = 11$ bit tentative calibration word $CALW$ is set to $2^{N_{DCO}-1}$ to make the DCO oscillate

reported in Fig. 8. The SE-ReDAC (Diff-ReDAC) area is only $5,030 \mu\text{m}^2$ ($7,800 \mu\text{m}^2$).

As shown in Fig. 7, the architecture of the test-chip entails the SE-ReDAC and the Diff-ReDAC core blocks along with their digital Calibration (CAL) units described in Sect.III and other ancillary blocks which are needed for testing, namely: a Sample-and-Hold Amplifier (SHA), to provide a low-impedance output suitable to drive external testing instruments, and a Digitally Controlled Oscillator (DCO) to generate the ReDAC clock signal and tune it depending on the digital calibration word from the CAL block, and a Direct Digital Synthesizer (SYNT) [21], to generate the digital input patterns needed for the static and dynamic characterization of the ReDAC. Finally, a Scan-chain (SCAN) interface is introduced to externally control and configure all the blocks. The silicon area occupied by each single block is reported in Tab.1

A. SAMPLE AND HOLD AMPLIFIER (SHA)

The SHAs are based on the standard architecture in Fig.9, which features two operational amplifiers (opamps) in the voltage follower configuration (schematic in Fig.10), a pass gate and a sampling capacitor $C_{SH} = 30 \text{ pF}$.

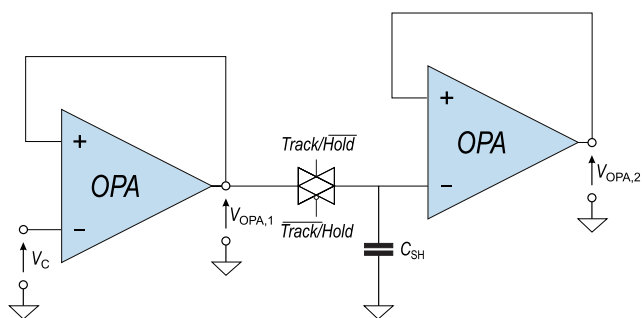


FIGURE 9. Sample-and-Hold Amplifier (SHA).

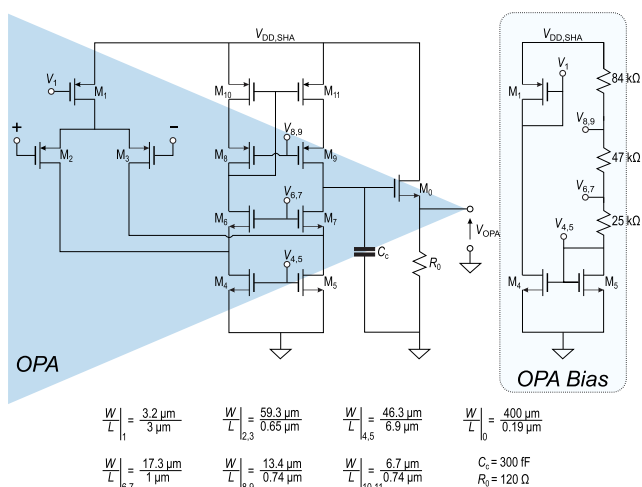


FIGURE 10. Schematic of the Folded Cascode amplifier employed in the Sample-and-Hold Amplifier.

For the SE-ReDAC, the SHA input is connected to the ReDAC capacitor to probe the voltage V_C , while the SHA output $V_{OPA,2}$ is connected to an analog output pad. The SHA is operated by the ReDAC control logic, which provides the *Track/Hold* signal to drive the pass-gate. In the Diff-ReDAC, two identical SHA blocks operated by the same *Track/Hold* signal are adopted for the positive and negative outputs.

The opamps in the SHAs are based on the folded cascode topology and have been designed to drive an output capacitive load up to 50 pF and to achieve a Gain-Bandwidth (GBW) product of 26 MHz, a slew-rate exceeding $18 \text{ V}/\mu\text{s}$, a 80 dB open-loop DC-gain and a total harmonic distortion (THD) of less than 0.01%, as demanded to settle within the ReDAC clock cycle with a DC accuracy exceeding 13 bit over the whole ReDAC output swing.

The op-amp performance are verified by post-layout simulations under process variations and mismatch, resulting in a 3σ spread of the DC-gain (GBW) of 2.1 dB (4.7 MHz) for process, and 0.2 dB (0.6 MHz) under mismatch.

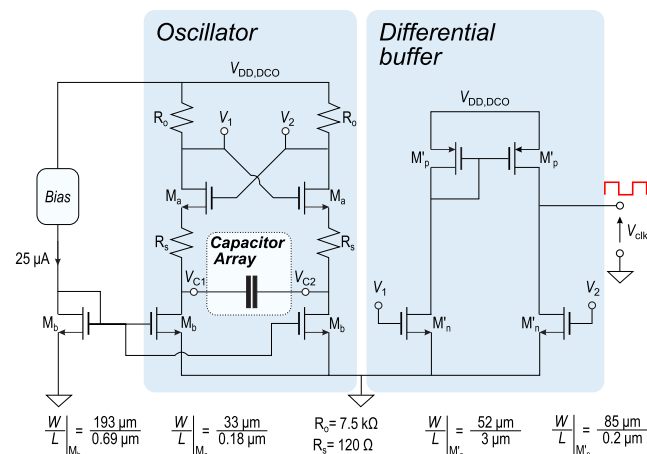


FIGURE 11. Schematic of the digitally controlled oscillator (DCO).

B. DIGITALLY CONTROLLED OSCILLATOR (DCO)

Unlike in [17], a DCO rather than a Voltage Controlled Oscillator (VCO) is adopted in this work. Even if this solution is much more area- and power-consuming compared to the VCOs, it has been chosen in our test chip to inherently avoid clock frequency variations due to leakage currents in the hold capacitor which stores the VCO analog control voltage in [17], and hence to suppress their effects on the ReDACs performance.

The DCOs adopted in the SE-ReDAC and in the Diff-ReDAC are based on the relaxation oscillator topology in Fig.12 with binary weighted capacitors driven by the calibration signals from the CAL blocks as demanded to tune the ReDACs clock frequency to enforce (3) with a resolution finer than the target ReDAC accuracy (11-bit for the SE-ReDAC, 13-bit for Diff-ReDAC). The DCO blocks

also generate the delayed clock clk_del , needed to implement the parasitic error suppression as in [16], by means of a digital delay line.

C. DIRECT DIGITAL SYNTHESIZER (SYNT)

A direct digital synthesizer (SYNT) is integrated on the ReDAC test-chip to generate the digital ramps and sine waves to be fed to the ReDACs inputs for static and dynamic testing.

The SYNT block is based on a classical phase-to-amplitude conversion architecture [21], in which the lookup table (LUT), is directly synthesized by combinational logic rather than by a read-only memory (ROM), resulting in a simpler and compact implementation.

The digital code $DATA$ provided to the ReDAC can be set via scan-chain to be a ramp (output of the phase accumulator) or a sine wave with configurable offset, amplitude and frequency for static and dynamic testing.

V. TEST SETUP AND EXPERIMENTAL RESULTS

The ReDAC has been tested under static and dynamic conditions by the setup in Fig.12. Here, the ReDAC power supply is provided by a source meter and the on-chip digital blocks are operated via the on-chip scan-chain by an FPGA connected to a PC by a serial data link. The output pad of the SHA is probed and acquired by a 16 bit Picoscope® 4262 oscilloscope connected to the test printed circuit board (PCB).

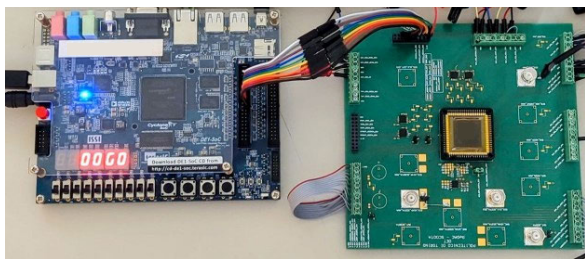


FIGURE 12. Experimental test setup.

The experimental characterization of the SE-ReDAC and of the Diff-ReDAC cells under static and dynamic conditions is presented in the following.

A. SE-REDAC

The results of the characterization of the SE-ReDAC circuit are reported in the following.

1) STATIC CHARACTERIZATION

The SE-ReDAC cell is tested for static characterization under the nominal conditions of 0.65 V supply at ambient temperature. Once the automatic calibration is run and completed, static characterization is performed and its nonlinearity is reported in Fig. 13(a), revealing a maximum (rms) INL of 1.26 LSB (0.42 LSB) and maximum (rms) DNL of 0.34 LSB (0.14 LSB).

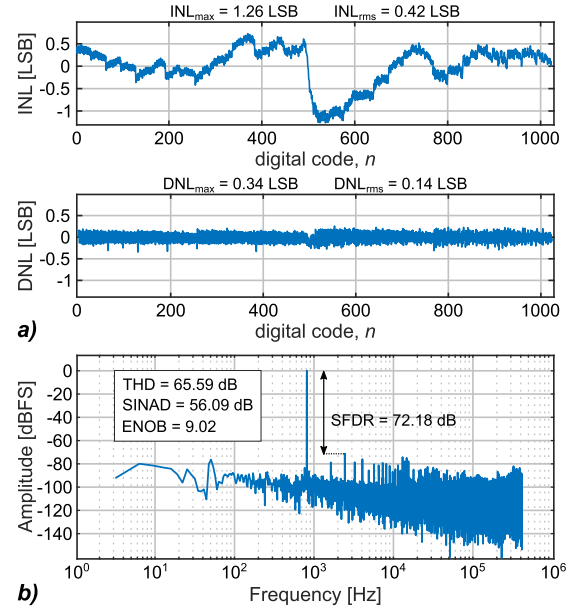


FIGURE 13. SE-ReDAC: static linearity (a) and output spectrum at 0.8 kHz-frequency, 90%-swing amplitude sine wave input (b).

2) DYNAMIC CHARACTERIZATION

The SE-ReDAC is then tested under dynamic conditions with a sine wave input at 0.8 kHz frequency, 90% swing amplitude. The output spectrum measured under these conditions is reported in Fig. 13(b) and reveals a SFDR of 72.18 dB, a THD of 65.59 dB and a SINAD of 56.09 dB, corresponding to 9.02 bit ENOB.

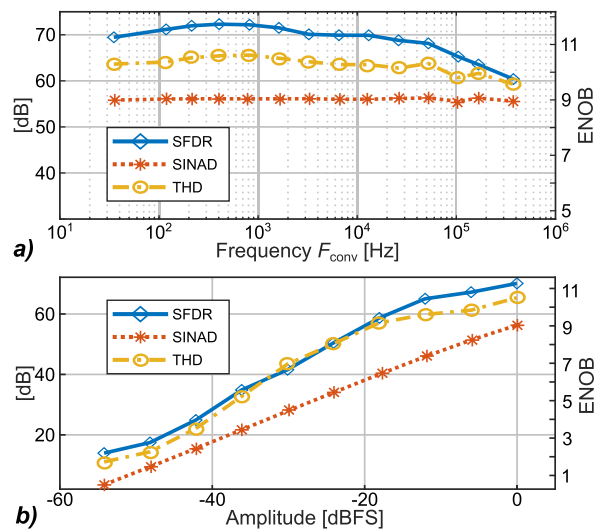


FIGURE 14. SE-ReDAC: dynamic ReDAC characterization versus input frequency at constant 90% swing amplitude (a), and versus input amplitude at 0.8 kHz input frequency (b).

The SE-ReDAC dynamic characterization at constant amplitude (90% full swing up to the Nyquist frequency) and at constant frequency (0.8kHz spanning the whole input

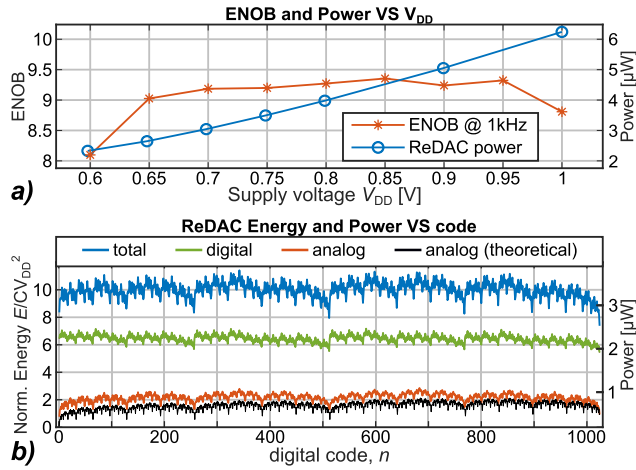


FIGURE 15. SE-ReDAC ENOB and power versus supply voltages (a) and energy per conversion/power versus digital code (b).

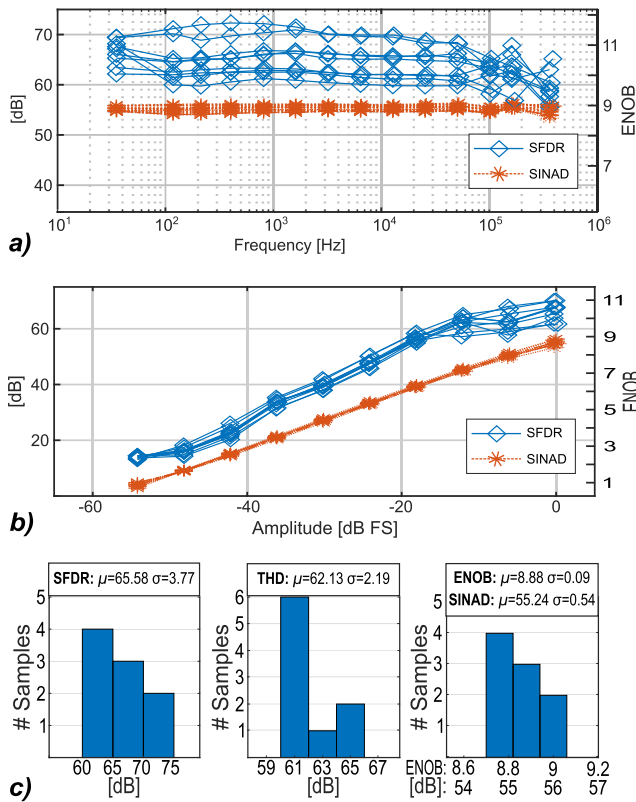


FIGURE 16. Multi-dice dynamic SE-ReDAC characterization over frequency, at 90%-swing amplitude (a), and over amplitude at 0.8 kHz input frequency. Distribution of the SE-ReDAC multi-dice dynamic performance at 0.8 kHz input frequency and 90%-swing amplitude (c).

swing) are reported in Fig. 14(a) and Fig. 14(b) respectively, revealing consistency in the whole frequency and amplitude range. The comparison of the SINAD and of the THD/SFDR plots suggests that the measured dynamic performance is noise-limited, while the SE-ReDAC linearity is very close to the 10-bit design target.

3) POWER CONSUMPTION AND VOLTAGE SCALING

Dynamic characterization of the SE-ReDAC under 1kHz sinewave, 90% swing, for supply voltages ranging in 0.6 V to 1 V reveal an ENOB equal or larger than 9 bit on a wide supply range, as reported in Fig. 15(a).

The SE-ReDAC average power for continuous conversion, under the same supply voltage sweep, is reported in Fig. 15(b) as well, revealing a power dissipation ranging from 2.3 μW to 6.2 μW and an optimum power-performance point between 0.65 V and 0.7 V.

In Fig. 7(b) the SE-ReDAC analog, digital and total power dissipation versus code is reported; the analog normalised energy per conversion nicely follows the predicted theoretical trend in (6), initially reported in [15], resulting in average analog (digital, total) power of 0.8 μW (2.5 μW , 3.3 μW).

4) MULTI-DICE MEASUREMENTS

The results of the SE-ReDAC dynamic characterization across nine dice up to the Nyquist rate (under 90% swing amplitude) is reported in Fig. 16(a).

The single frequency in-band characterization (0.8 kHz, 90% swing) performance distribution in Fig. 16(b) reveals a mean (standard deviation) of 65.58 dB (3.77 dB) for SFDR, 82.13 dB (2.19 dB) for THD and 55.24 dB (0.54 dB) for SINAD, resulting in a highly consistent effective resolution (ENOB) of 8.88 bit across the samples, with a standard deviation of just 0.09 bit.

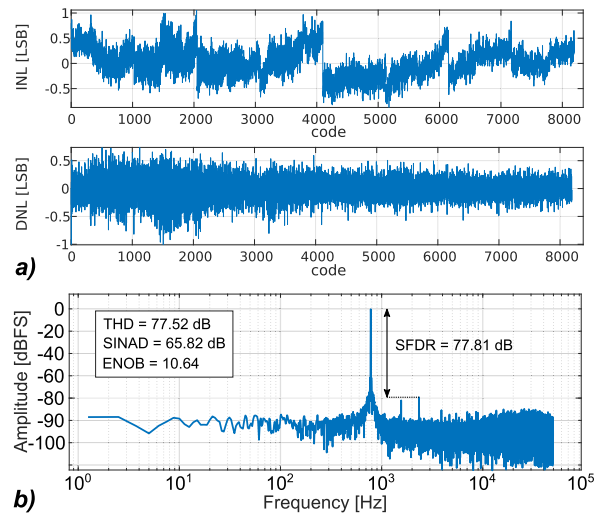


FIGURE 17. Diff-ReDAC: static linearity (a), and 0.8 kHz, 90% swing spectrum (b).

B. DIFF-REDAC

The results of the characterization of the Diff-ReDAC circuit are reported in the following.

1) STATIC CHARACTERIZATION

The results of the Diff-ReDAC static characterization under 0.6 V power supply and at ambient temperature are reported

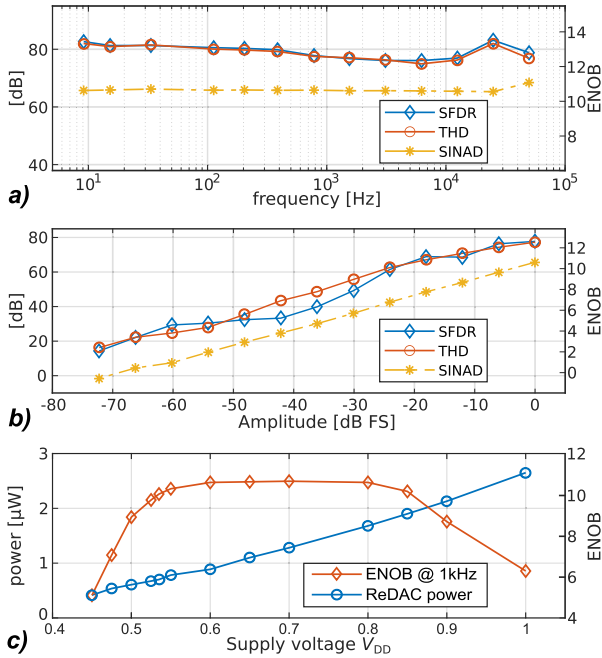


FIGURE 18. Diff-ReDAC: dynamic characterization versus input sinewave frequency at constant 90%-swing amplitude (a), versus input sinewave amplitude at constant 0.8 kHz input frequency (b), ENOB and power consumption at different power supply voltages, for a fixed sinewave input at 800 Hz frequency, 90%-swing amplitude (c).

in Fig. 17(a) and reveal a maximum (rms) INL of 1.07 LSB (0.28 LSB) and a maximum (rms) DNL of 0.96 LSB (0.20 LSB).

2) DYNAMIC CHARACTERIZATION

The spectrum of the Diff-ReDAC output voltage under a 0.8 kHz, 90% swing sine is reported in Fig. 17(b) and reveals a SFDR (THD) of 77.81 dB (77.52 dB) and a 65.82 dB SINAD, resulting in an effective resolution of 10.64 ENOB. Based on Fig. 18(a) and Fig. 18(b), the Diff-ReDAC shows consistent performance up to the Nyquist rate and over the whole input swing. Comparing the SINAD plot with the THD and SFDR plots it can be observed that the measured Diff-ReDAC dynamic performance is noise-limited, while its linearity is close to the 13-bit design target.

3) POWER CONSUMPTION AND VOLTAGE SCALING

The dynamic performance/power tradeoff for the Diff-ReDAC converter has been tested at 800 Hz, 90 % swing sine under different supply voltages (from 0.45 V to 1 V). The results of the test, reported in Fig. 18(c) reveal an ENOB larger than 10 bits over most of the supply range and with a power dissipation ranging from 420 nW to 2,650 nW (880 nW under 0.6 V nominal supply).

4) MULTI-DICE MEASUREMENTS

The multi-dice validation across 12 samples is performed under 90 % input sinewave and up to Nyquist (Fig. 19(a)) and

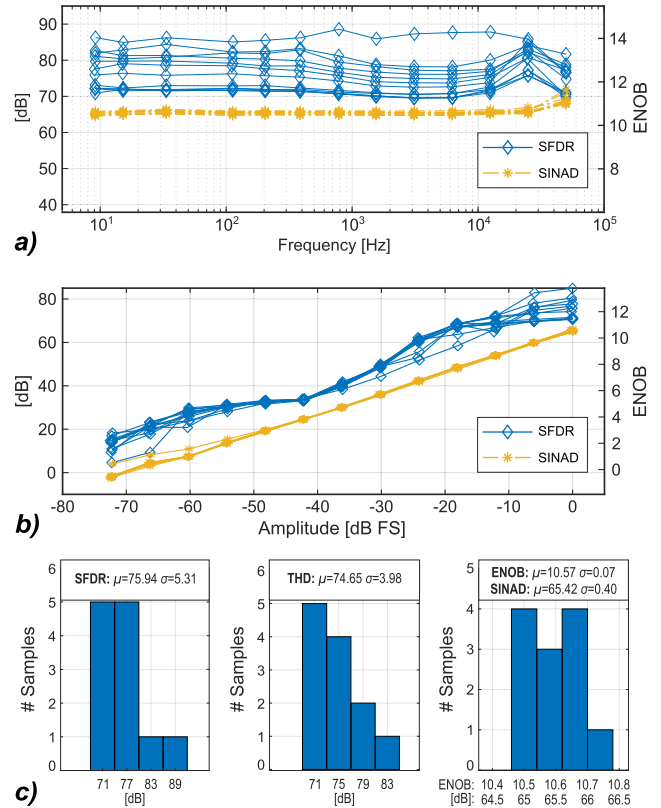


FIGURE 19. Multi-dice dynamic Diff-ReDAC characterization over frequency at 90%-swing amplitude (a), and over amplitude, at 0.8 kHz input frequency (b). Distribution of the Diff-ReDAC multi-dice dynamic performance at 0.8 kHz input frequency, 90% swing amplitude (c).

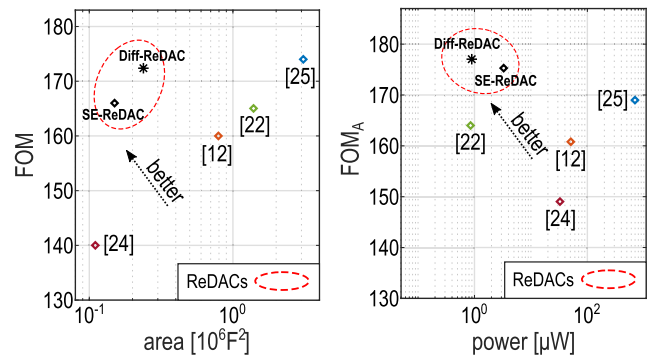


FIGURE 20. Schreier FOM vs. area and area-normalised FOM_A vs power: comparison with the state of the art.

at constant 0.8 kHz frequency spanning the whole input range (Fig. 19(b)).

The histograms of the main performance, which are reported in Fig. 19(c), reveal a mean SFDR of 75.94 dB with a standard deviation of 5.31 dB, a mean THD of 74.65 dB with a standard deviation of 3.98 dB and a mean SINAD of 65.42 dB with a standard deviation of only 0.40 dB, resulting in a very consistent Diff-ReDAC effective resolution (ENOB) of 10.57 bit with only 0.07 bit standard deviation.

TABLE 2. DAC performance comparison.

	This Work		[12]	[20]	[18]	[22]	[23]	[24]	[25]
Tech. (nm)	180		40	40	180	180	180	350	180
Type	SE-ReDAC	Diff-ReDAC	DDPM	ReDAC	ReDAC	cap+mos	R-string	curr. steer.	$\Sigma\Delta$
validation	meas.		meas.	sim.	sim.	meas.	meas.	meas.	meas.
Area ($10^6 \mu\text{m}^2$)	0.00503	0.00780	0.00127	0.00091	0.01359 ^a	0.045 ^b	0.15	0.014	0.10 ^c
Area (10^6F^2)	0.15	0.24	0.79	0.57	0.42	1.39	4.6	0.11	3.08
Resolution (bit)	10	13	12	10	10	10	12	9	N/A
Sample rate (kS/s)	880	100	110	400	1,450	200	72 ^d	111	40 ^e
Supply (V)	0.65	0.6	1	0.6	0.7	0.6	1.8	3.3	1.8
Min.supply (V)	0.6	0.45	0.7	N/A	N/A	N/A	1.8	N/A	N/A
INL (LSB)	1.26	1.07	3	0.33	1.01	0.56	0.54	1.6	N/A
DNL (LSB)	0.34	0.96	1	0.2	0.45	0.32	0.26	0.8	N/A
SFDR (dB)	72.18	77.81	85	76.8	59.3	71	N/A	N/A	N/A
THD (dB)	65.59	77.52	85	66.7	59.2	N/A	N/A	N/A	N/A
SINAD (dB) (peak)	56.09	65.82	72	61.0	58.5	56.43	N/A	48 ^b	103 ^f
ENOB (peak)	9.02	10.64	11.6	9.9	9.4	9.08	N/A	8 ^b	16.8
Power (μW)	3.3	0.88	50.8	0.44	9.15	0.85 ^b	875 ^b	33	700 ^g
[†] FOM(dB)	166	172	160	176	166	165	N/A	140	174 ^f
[‡] FOM _A (dB)	175	178	161	178	170	164	N/A	149	169

[†]FOM = $10 \log_{10} \left(\frac{2^{2 \cdot \text{ENOB}_{BW}}}{P} \right)$ [‡]FOM_A = FOM + $10 \log_{10}(1/A_F)$ being A_F the F-normalised area ^aincludes part of the calibration ^bbased on text and figures ^c not including reconstruction filter ^dfrom row-line time ^etwice the signal bandwidth ^fA-weighted ^ganalog power only.

C. PERFORMANCE COMPARISON

The performance of the ReDACs presented in this paper is discussed and compared with the state of the art in Tab. 2. From the comparison it can be observed that the proposed SE-ReDAC achieves from $2.8 \times$ [18] to $3.8 \times$ [20] smaller normalized area compared to previously reported ReDACs and the second smallest total normalised area among all (30% larger than the minimum [24], which achieves lower resolution and sample rate).

Compared to DDPM DACs [11], the SE-ReDAC requires a much lower clock frequency to operate at the same bandwidth, while keeping consistent dynamic performance across the whole frequency range (only 0.08 bit ENOB degradation is observed at the Nyquist-rate, compared to the 6.1 bit difference in [11]).

Based on these results, the SE-ReDAC achieves a very competitive energy efficiency figure of merit (FOM) and area-normalized figure of merit (FOM_A) of 166 dB and 175 dB, respectively (see Fig. 20), comparable only with sigma-delta audio DACs [25], which achieves 7.8 more (A-weighted) effective bits with a $20 \times$ smaller bandwidth at the cost of $212 \times$ more power and $19.9 \times$ more area. The proposed ReDAC is also operating at the lowest voltage (same as [20], [22]).

Compared to silicon-proven DACs reported in Tab. 2, the Diff-ReDAC achieves the second smallest absolute area ($6.1 \times$ more than [11], fabricated in a finer node) and the second smallest normalised area ($2.2 \times$ the area of [24], which has comparable sample rate and 2.6 less ENOB) and is $19 \times$ smaller than [23]. Moreover, our Diff-ReDAC can operate down to the lowest supply voltage (0.45 V) featuring energy-quality scaling.

The Diff-ReDAC achieves the second best energy-efficiency figure of merit FOM of 172 dB (2 dB less than the FOM of the oversampled converter [25], which is

based on A-weighted ENOB and has a $795 \times$ larger power consumption) and the best area-normalised FOM_A of 178 dB (9 dB more than [25] and 29 dB more than the current-steering DAC [24]).

VI. CONCLUSION

The design and silicon verification of a single-ended and of a differential ReDACs in 180 nm featuring digital self-calibration and parasitics-induced error suppression have been presented. The proposed SE-ReDAC occupies just $5,030 \mu\text{m}^2$ and draws $3.3 \mu\text{W}$ from a 0.65 V power supply voltage at 880 kS/s and 9.02 ENOB, achieving competitive energy efficiency, and area-normalized energy efficiency figures of merit of 166 dB and 175 dB, respectively. On the other hand, the Diff-ReDAC design operates down to 0.45 V power supply and with $7,800 \mu\text{m}^2$ area and 880 nW power consumption at 100 kS/s and 10.64 ENOB, achieves a FOM of 172 dB and the best reported area normalized energy efficiency FOM_A of 178 dB. Such remarkable results highlight the inherent advantages and the potential of the ReDAC technique in the design of compact, very low power, low design effort, robust integrated DACs for medium resolution and kS/s-to-MS/s sample rate applications, thus meeting the requirements of low-cost analog interfaces for next-generation IoT applications and biosensors.

REFERENCES

- [1] M. Alioto, "From less batteries to battery-less alert systems with wide power adaptation down to nWs—toward a smarter, greener world," *IEEE Design Test*, vol. 38, no. 5, pp. 90–133, Oct. 2021.
- [2] M. Cho, S. Oh, Z. Shi, J. Lim, Y. Kim, S. Jeong, Y. Chen, D. Blaauw, H.-S. Kim, and D. Sylvester, "17.2 a 142nW voice and acoustic activity detection chip for mm-scale sensor nodes using time-interleaved mixer-based frequency scanning," in *IEEE Int. Solid-State Circuits Conf. (ISSCC) Dig. Tech. Papers*, San Francisco, CA, USA, Feb. 2019, pp. 278–280, doi: 10.1109/ISSCC.2019.8662540.

- [3] S. Carrara, "Body dust: Well beyond wearable and implantable sensors," *IEEE Sensors J.*, vol. 21, no. 11, pp. 12398–12406, Jun. 2021.
- [4] M. Dei, J. Aymerich, M. Piotta, P. Bruschi, F. J. del Campo, and F. Serra-Graells, "CMOS interfaces for Internet-of-Wearables electrochemical sensors: Trends and challenges," *Electronics*, vol. 8, no. 2, p. 150, Jan. 2019, doi: [10.3390/ELECTRONICS8020150](https://doi.org/10.3390/ELECTRONICS8020150).
- [5] S.-J. Kweon, A. K. Rafi, S.-I. Cheon, M. Je, and S. Ha, "On-chip sinusoidal signal generators for electrical impedance spectroscopy: Methodological review," *IEEE Trans. Biomed. Circuits Syst.*, vol. 16, no. 3, pp. 337–360, Jun. 2022, doi: [10.1109/TBCAS.2022.3171163](https://doi.org/10.1109/TBCAS.2022.3171163).
- [6] K. Kim, S. Kim, and H.-J. Yoo, "Design of sub-10- μ W sub-0.1% THD sinusoidal current generator IC for bio-impedance sensing," *IEEE J. Solid-State Circuits*, vol. 57, no. 2, pp. 586–595, Feb. 2022, doi: [10.1109/JSSC.2021.3100716](https://doi.org/10.1109/JSSC.2021.3100716).
- [7] J. Xu and Z. Hong, "Low power bio-impedance sensor interfaces: Review and electronics design methodology," *IEEE Rev. Biomed. Eng.*, vol. 15, pp. 23–35, 2022, doi: [10.1109/RBME.2020.3041053](https://doi.org/10.1109/RBME.2020.3041053).
- [8] R. Rubino, S. Carrara, and P. Crovetto, "Direct digital sensing potentiostat targeting body-dust," in *Proc. IEEE Biomed. Circuits Syst. Conf. (BioCAS)*, Taipei, Taiwan, Oct. 2022, pp. 280–283, doi: [10.1109/BIO-CAS54905.2022.9948649](https://doi.org/10.1109/BIO-CAS54905.2022.9948649).
- [9] M. ElAnsary, J. Xu, J. S. Filho, G. Dutta, L. Long, C. Tejeiro, A. Shoukry, C. Tang, E. Kilinc, J. Joshi, P. Sabetian, S. Unger, J. Zariffa, P. Yoo, and R. Genov, "Bidirectional peripheral nerve interface with 64 second-order opamp-less $\Delta\Sigma$ ADCs and fully integrated wireless power/data transmission," *IEEE J. Solid-State Circuits*, vol. 56, no. 11, pp. 3247–3262, Nov. 2021, doi: [10.1109/JSSC.2021.3113354](https://doi.org/10.1109/JSSC.2021.3113354).
- [10] P. Li, T. R. Molderez, D. H. Villamor, A. PrévotEAU, and M. Verhelst, "A 96-channel 40nm CMOS potentiostat for parallel experiments on microbial electrochemical systems," *IEEE Trans. Circuits Syst. I, Reg. Papers*, vol. 70, no. 1, pp. 114–127, Jan. 2023, doi: [10.1109/TCSI.2022.3214470](https://doi.org/10.1109/TCSI.2022.3214470).
- [11] P. S. Crovetto, "All-digital high resolution D/A conversion by dyadic digital pulse modulation," *IEEE Trans. Circuits Syst. I, Reg. Papers*, vol. 64, no. 3, pp. 573–584, Mar. 2017, doi: [10.1109/TCSI.2016.2614231](https://doi.org/10.1109/TCSI.2016.2614231).
- [12] O. Aiello, P. Crovetto, and M. Alioto, "Standard cell-based ultra-compact DACs in 40-nm CMOS," *IEEE Access*, vol. 7, pp. 126479–126488, 2019, doi: [10.1109/ACCESS.2019.2938737](https://doi.org/10.1109/ACCESS.2019.2938737).
- [13] P. Toledo, R. Rubino, F. Musolino, and P. Crovetto, "Re-thinking analog integrated circuits in digital terms: A new design concept for the IoT era," *IEEE Trans. Circuits Syst. II, Exp. Briefs*, vol. 68, no. 3, pp. 816–822, Mar. 2021, doi: [10.1109/TCSII.2021.3049680](https://doi.org/10.1109/TCSII.2021.3049680).
- [14] P. S. Crovetto, "A digital-based virtual voltage reference," *IEEE Trans. Circuits Syst. I, Reg. Papers*, vol. 62, no. 5, pp. 1315–1324, May 2015, doi: [10.1109/TCSI.2015.2402991](https://doi.org/10.1109/TCSI.2015.2402991).
- [15] P. S. Crovetto, R. Rubino, and F. Musolino, "Relaxation digital-to-analogue converter," *Electron. Lett.*, vol. 55, no. 12, pp. 685–688, Jun. 2019, doi: [10.1049/EL.2019.0784](https://doi.org/10.1049/EL.2019.0784).
- [16] R. Rubino, P. S. Crovetto, and F. Musolino, "FPGA-based relaxation D/A converters with parasitics-induced error suppression and digital self-calibration," *IEEE Trans. Circuits Syst. I, Reg. Papers*, vol. 68, no. 6, pp. 2494–2507, Jun. 2021, doi: [10.1109/TCSI.2021.3064419](https://doi.org/10.1109/TCSI.2021.3064419).
- [17] P. S. Crovetto, R. Rubino, and F. Musolino, "Relaxation digital-to-analog converter with foreground digital self-calibration," in *Proc. IEEE Int. Symp. Circuits Syst. (ISCAS)*, Seville, Spain, Oct. 2020, pp. 1–5, doi: [10.1109/ISCAS45731.2020.9180696](https://doi.org/10.1109/ISCAS45731.2020.9180696).
- [18] R. Rubino, F. Musolino, and P. Crovetto, "Relaxation digital-to-analog converter with radix-based digital correction," in *Proc. IEEE Int. Symp. Circuits Syst. (ISCAS)*, Austin, TX, USA, May 2022, pp. 1402–1406, doi: [10.1109/ISCAS48785.2022.9937502](https://doi.org/10.1109/ISCAS48785.2022.9937502).
- [19] R. Rubino, F. Musolino, Y. Chen, A. Richelli, and P. Crovetto, "A 880 nW, 100 kS/s, 13 bit differential relaxation-DAC in 180 nm," in *Proc. 18th Conf. Ph.D. Res. Microelectron. Electron. (PRIME)*, Valencia, Spain, Jun. 2023, pp. 269–272, doi: [10.1109/PRIME58259.2023.10161768](https://doi.org/10.1109/PRIME58259.2023.10161768).
- [20] R. Rubino, P. S. Crovetto, and O. Aiello, "Design of relaxation digital-to-analog converters for Internet of Things applications in 40nm CMOS," in *Proc. IEEE Asia-Pacific Conf. Circuits Syst. (APCCAS)*, Nov. 2019, pp. 13–16.
- [21] J. Zhang, R. Zhang, and G. Li, *High-Speed and High-Performance Direct Digital Frequency Synthesizer Design*. Singapore: Springer, Mar. 2022.
- [22] H. Zhang, H. Zhang, Q. Sun, J. Li, X. Liu, and R. Zhang, "A 0.6-V 10-bit 200-kS/s SAR ADC with higher side-reset-and-set switching scheme and hybrid CAP-MOS DAC," *IEEE Trans. Circuits Syst. I, Reg. Papers*, vol. 65, no. 11, pp. 3639–3650, Nov. 2018, doi: [10.1109/TCSI.2018.2853043](https://doi.org/10.1109/TCSI.2018.2853043).
- [23] H.-C. Seol, S.-K. Hong, and O.-K. Kwon, "An area-efficient high-resolution resistor-string DAC with reverse ordering scheme for active matrix flat-panel display data driver ICs," *J. Display Technol.*, vol. 12, no. 8, pp. 828–834, Aug. 2016, doi: [10.1109/JDT.2016.2526042](https://doi.org/10.1109/JDT.2016.2526042).
- [24] H.-S. Kim, J.-Y. Jeon, S.-W. Lee, J.-H. Yang, S.-T. Ryu, and G.-H. Cho, "A 0.014 mm² 9b switched-current DAC for AMOLED mobile display drivers," in *Proc. IEEE Int. Solid-State Circuits Conf.*, San Francisco, CA, USA, Feb. 2011, pp. 316–318, doi: [10.1109/ISSCC.2011.5746335](https://doi.org/10.1109/ISSCC.2011.5746335).
- [25] H. Westerveld, D. Schinkel, and E. van Tuijl, "15.3 a 115dB-DR audio DAC with -61dBFS out-of-band noise," in *IEEE Int. Solid-State Circuits Conf. (ISSCC) Dig. Tech. Papers*, San Francisco, CA, USA, Feb. 2015, pp. 1–3, doi: [10.1109/ISSCC.2015.7063033](https://doi.org/10.1109/ISSCC.2015.7063033).
- [26] M. Seok, G. Kim, D. Blaauw, and D. Sylvester, "A portable 2-transistor picowatt temperature-compensated voltage reference operating at 0.5 V," *IEEE J. Solid-State Circuits*, vol. 47, no. 10, pp. 2534–2545, Oct. 2012, doi: [10.1109/JSSC.2012.2206683](https://doi.org/10.1109/JSSC.2012.2206683).



ROBERTO RUBINO (Member, IEEE) received the Laurea degree in electronic engineering and the Ph.D. degree (cum laude) from the Politecnico di Torino, Turin, Italy, in 2019 and 2023, respectively, developing ultra-low-voltage and ultra-low-power digital-intensive analog interfaces targeting the Internet of Things (IoT) and next-generation biosensors. He is currently with Analog Devices as a Senior Mixed-Signal Design Engineer developing digital healthcare (DHC) devices. His research interests include microelectronics design and modeling of analog and mixed-signal sensing interfaces. He has been awarded with the Gold Leaf Prize (top 10% Ph.D. students papers) at the 18th International Conference on Ph.D. Research in Microelectronics and Electronics (PRIME), in 2023.



FRANCESCO MUSOLINO (Member, IEEE) was born in Turin, Italy, in 1972. He received the Laurea and Ph.D. degrees in electronic engineering from the Politecnico di Torino, Turin, in 1999 and 2003, respectively. He is currently a Researcher with the Department of Electronics and Telecommunications (DET), Politecnico di Torino, where he teaches courses on power electronics and electronics for electric drives. His research interests include electronics for power conversion and motor drive applications, mixed-signal circuits, electromagnetic compatibility at the system levels, the analysis, modeling, and experimental characterization of electromagnetic compatibility problems at the printed circuit board and package level.



PEDRO TOLEDO (Member, IEEE) received the B.Sc. degree in electronic engineering from the Universidade Federal de Pernambuco (UFPE), Recife, Brazil, in 2010, the M.Sc. degree in microelectronics from the Universidade Federal do Rio Grande do Sul (UFRGS), Porto Alegre, Brazil, in 2015, and the joint Ph.D. degree from the Politecnico di Torino and the Universidade Federal do Rio Grande do Sul, working with digital-based analog processing for IoT applications in 2021. He completed the IC-Brazil Program, in 2011. He is currently a RF/AMS Circuit Designer with Synopsys with sub-10 nm CMOS technologies (FinFET, GAA, and Nanosheet) for high-performance computers. He has also won the best 2015 master's and 2021 Ph.D. thesis in the design, CAD, and IC Test Category from Brazilian Society of Microelectronics (SBMICRO). His research interests include electrical engineering, focusing on analog/RF CMOS design and microelectronic education. He is a member of the IEEE Circuits and Systems Society and the IEEE Solid-State Circuits Society.



YONG CHEN (Senior Member, IEEE) received the B.Eng. degree in electronic and information engineering from the Communication University of China (CUC), Beijing, China, in 2005, and the Ph.D. (Eng.) degree in microelectronics and solid-state electronics from the Institute of Microelectronics of Chinese Academy of Sciences (IMECAS), Beijing, in 2010. From 2010 to 2013, he was a Postdoctoral Researcher with the Institute of Microelectronics, Tsinghua University, Beijing.

From 2013 to 2016, he was a Research Fellow with VIRTUS/EEE, Nanyang Technological University, Singapore. Then, he was an Assistant Professor, from 2016 to 2022, and an Associate Professor, from 2022 to 2024, with the State Key Laboratory of Analog and Mixed-Signal VLSI (AMS), University of Macau, Macau, China. In 2024, he joined the Department of Electronic Engineering, Tsinghua University, where he is currently an Associate Professor. His research interest includes integrated circuit designs involving analog/mixed-signal/RF/mm-wave/sub-THz/wireline. He was a recipient of the “Haixi” (three places across the Straits) postgraduate integrated circuit design competition (Second Prize) in 2009, the co-recipient of the Best Paper Award at the IEEE Asia–Pacific Conference on Circuits and Systems (APCCAS), in 2019, the Best Student Paper Award (Third Place) at the IEEE Radio Frequency Integrated Circuits (RFIC) Symposium, in 2021, Macao Science and Technology Invention Award (First Prize), in 2020, and Macao Science and Technology Invention Award (Second Prize), in 2022, and Gold Leaf Prize (Top 10% Papers) at the 18th International Conference on Ph.D. Research in Microelectronics and Electronics (PRIME), in 2023. He was recognized as the top five Associate Editors, in 2020, the five highest-performing Associate Editors, in 2021, one of the three best Associate Editor, in 2022, one of the three best Reviewer, in 2022, of IEEE TRANSACTIONS ON VERY LARGE SCALE INTEGRATION (VLSI) SYSTEMS and one of the inaugural SSCS Reviewer Rewards of IEEE Solid-State Circuits Society (SSCS), in 2023. He has been serving as an Associate Editor for IEEE TRANSACTIONS ON VERY LARGE SCALE INTEGRATION (TVLSI) SYSTEMS, since 2019, has been a Subject Editor, since 2022, for Circuits & Systems of *IET Electronics Letters* (EL) and an Associate Editor (2020–2023) of *IET EL*, an Editor of *International Journal of Circuit Theory and Applications* (IJCTA), since 2020, a Guest Editor (2022–2023) of IEEE TRANSACTIONS ON CIRCUITS AND SYSTEMS—I: REGULAR PAPERS, in 2022, and a Guest Editor (2021–2022) of IEEE TRANSACTIONS ON CIRCUITS AND SYSTEMS—II: EXPRESS BRIEFS. He serves as the Vice-Chair (2019–2021) and the Chair (2021–2023) of IEEE Macau CAS Chapter and the technical program committees of several international conferences.



ANNA RICELLI (Senior Member, IEEE) was born in Brescia, Italy, in 1974. She received the D.Eng. and Ph.D. degrees in electronic instrumentation from the University of Brescia, Italy, in 2000 and 2004, respectively. She is currently an Associate Professor with the Department of Information Engineering, University of Brescia. Her research interests include electromagnetic interference analysis in integrated circuits, integrated voltage converters based on capacitors or

on inductors, and the design of ultra-low voltage analog circuits. She is the author of many international scientific publications, including articles in journals and in conference proceedings, and of several international patents.



PAOLO S. CROVETTI (Senior Member, IEEE) was born in Turin, Italy, in 1976. He received the Laurea (summa cum laude) and Ph.D. degrees in electronic engineering from the Politecnico di Torino, Turin, in 2000 and 2003, respectively. He is currently an Associate Professor with the Department of Electronics and Telecommunications (DET), Politecnico di Torino, where he leads a research group in analog, mixed-signal, and power microelectronics with several international

collaborations and teaches courses on basic and automotive electronics. He has co-authored more than 110 papers appearing in journals and international conference proceedings. In 2009 and 2019, he was co-recipient of the Excellent Paper Award of the EMC’09 Kyoto Symposium and of the Best Student Paper Award of the International Symposium of Circuits and Systems ICECS 2019. His main research interests include integrated circuit design and electromagnetic compatibility (EMC), non-conventional digital-based information processing techniques and ultra-low-voltage, and ultra-low-power IC design for the Internet of Things. He was a co-recipient of the Gold Leaf Prize (Top 10% Papers) at the 18th International Conference on Ph.D. Research in Microelectronics and Electronics (PRIME), in 2023, of the Best Student Paper Award at the 26th IEEE International Conference on Electronics Circuits and Systems (ICECS), in 2018, and of the Excellent Paper Award at the 2009 International Symposium on EMC, Kyoto. He serves as the Editor-in-Chief for *IET Electronics Letters* and as a Senior Associate Editor for IEEE TRANSACTIONS ON CIRCUITS AND SYSTEMS—PART I: REGULAR PAPERS and of IEEE TRANSACTIONS ON VERY LARGE SCALE OF INTEGRATION (VLSI) SYSTEMS and is the Co-Chair of the EMC Society Italy Chapter.

...